11 Particle Physics with CMS

C. Amsler, A. Dorokhov, C. Hörmann, K. Prokofiev, H. Pruys, C. Regenfus,
P. Robmann, T. Speer, and S. Steiner

in collaboration with:
ETH-Zürich, Paul Scherrer Institut (PSI), Universität Basel and the CMS Collaboration.

We participate in the CMS experiment at the Large Hadron Collider (LHC) where we concentrate on physics involving the b-quark, e.g. b-quark production associated with the formation of Higgs bosons, t-quark decays, and spectroscopy of B mesons. The most interesting events at LHC will contain one or several b-jets originating from the decay of B mesons, with typical mean free paths of a few mm. To allow for efficient tagging of B mesons among the large background of light quark and gluon jets, the detection system has to follow particles towards the primary vertex. The silicon pixel detector we are developing is the closest detector to the interaction point, located only 4 cm from the beam-beam interaction point. The extremely high particle flux near the primary vertex ($\sim$ 1000 particles every 25 ns) requires the innermost tracking layers to be composed of pixel devices delivering 3D coordinates with high resolution and no ambiguity. Furthermore, the radiation dose to the nearest detector will approach 10^6 Gy (corresponding to 6×10^{14} hadrons /cm^2) after 10 years of LHC operation. This is about 10^6 more than for detectors developed earlier for space research.

Our group contributes to the design, construction and test of the pixel sensors, the readout chips and the mechanical support structure, and we are also involved in the event reconstruction software.

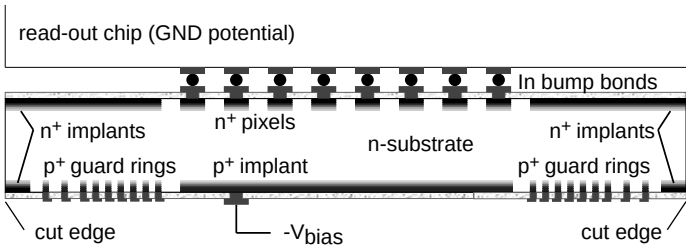

Figure 11.1: *Design of a sensor connected to the readout chip. The bias voltage is applied to the backside.*

11.1 Pixel sensors

The barrel pixel detector consists in three concentric cylindrical layers, 53 cm long with radii of 4.4, 7.3 and 10.2 cm. The layers contain some 3×10^7 silicon pixels. Coverage in the beam direction is achieved with forward/backward wheels provided by the U.S. participants. The pixel modules consist of thin, segmented sensor plates with highly integrated readout chips connected by the indium bump bonding technique. Figure 11.1 shows a sketch of the sensor/chip assembly. The pixel size was recently reduced from 150 $\times$ 150 μm^2 to 125 $\times$ 125 μm^2 and rectangular pixels of 150 $\times$ 100 μm^2 are being considered for the final design. The analogue signals are read out to determine the coordinates more accurately, using charge sharing between adjacent pixels.

For n^+ implants in n-material the pixels have to be isolated from one another. This is usually done with one or several narrow p^+-rings around each pixel (the so-called p-stop rings). To avoid excessive charging of an unbonded pixel (one with poor indium connection to the chip) leading to local

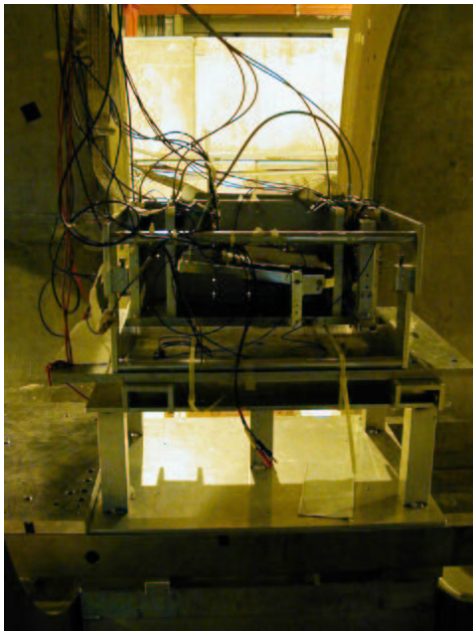

Figure 11.2: *Setup for the sensors test. The pixel detectors are located at the center of the silicon telescope. The two supraconductive coils are visible at the edges of the picture.*

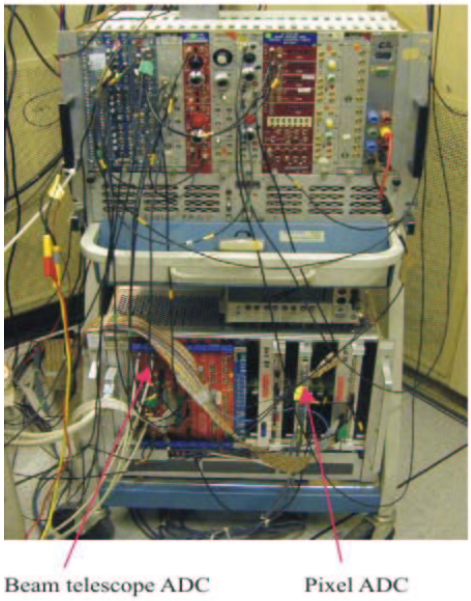

Figure 11.3: *Readout and control system.*

discharges and momentary failures of whole pixel clusters, the resistance between pixels should remain finite. A narrow resistive path between the pixels would prevent the pixels from charging up. This is accomplished by small openings in the p-rings which lead to atoll-like structures made of one or several rings surrounding each pixel (see fig. 11.6) below. More details can be found in previous annual reports, in the technical design report [1] and in a recent PhD thesis [2].

In 2002 we ordered with CiS Erfurt a batch of sensors with various atoll designs, some oxygenated (oxygen is known to reduce the acceptor concentration after type inversion and hence also the required depletion voltage). In some of the sensors the p-stop rings were missing. Instead, the p implant was not spatially defined by a mask, but sprayed over the whole wafer with moderate concentration.

A first test of this batch was performed by the Zurich group in July 2002 using 225 GeV pions from the CERN-SPS. The purpose of the test was to measure (i) the position resolution, (ii) the charge collection efficiency, and (iii) the Lorentz deflection angle in the 4 T field foreseen at CMS. The pixel detector was located at the center of our microstrip telescope [3], so that pions would traverse the detector at a grazing angle $\alpha = 15^\circ$ (fig. 11.2). Our telescope is made of 8 layers of x and y silicon microstrips (50 μm pitch size). Through charge division between neighbouring strips the telescope is capable of measuring the space coordinates of an incident charged particle with an r.m.s. resolution of 1 μm [3]. A fast trigger diode (less than 20ns rise time) provided the trigger. The silicon sensor was bump bonded to the readout chip (PSI30, DMILL/Honeywell) and was read out through VME ADC's by a LabView program. The data acquisition system is shown in fig. 11.3.

The apparatus was immersed in a longitudinal magnetic field provided by two Helmholtz coils to measure the Lorentz angle Θ_L: due to deflection in the magnetic field the charge carriers do not move along the electric field lines but drift at an angle Θ_L towards adjacent pixels. The charge deposit is therefore shared among (mostly two) adjacent pixels. The Lorentz angle can be measured by finding the coordinate z of the pixel row for which the charge collected between the main and adjacent pixels are equal (fig. 11.5). This corresponds to charge reaching the readout surface between two pixels. The coordinate Δy of the impinging track is determined by the telescope and Θ_L can be calculated from the relation tanΘ_L = Δy/z tanα. Note that for irradiated pixels after type inversion the depletion layer grows from the readout side (as shown in fig. 11.5). The depletion thickness can be determined from the length of the hit pixels along the

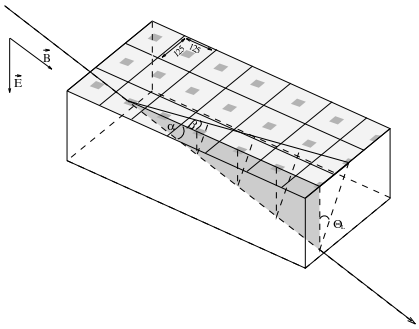

Figure 11.4: *Sketch of the pixel detector traversed by a charged particle under the grazing angle α. The Lorentz angle is denoted by Θ_L.*

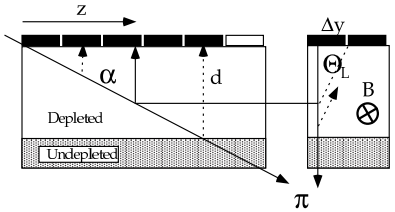

Figure 11.5: *Determination of the Lorentz angle Θ_L (see text).*

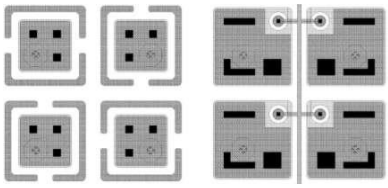

Figure 11.6: *The two pixel layouts tested in 2002: p-stop (left) and p-spray (right).*

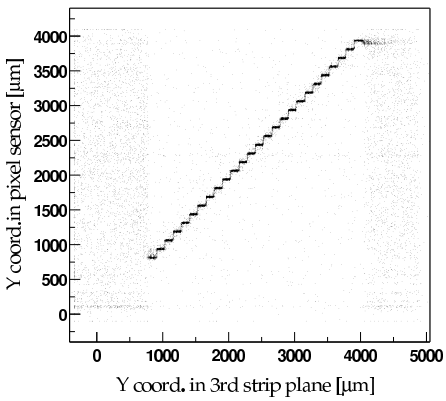

Figure 11.7: *Vertical hit coordinate in the third strip detector vs. vertical hit coordinate in the pixel sensors. The steps are due to the much smaller pitch of the microstrip detector. The dark bands left and right are due to open readout channels.*

incident direction. Similar studies were performed earlier by our group [2; 4]. However, several design parameters for the sensors have changed since then: we have now somewhat smaller pixel sizes, atoll-like p-stop rings and a different supplier. Also the pixels are now bump-bonded to a semifinal version of the readout chip.

Data were collected with two detectors made of 32 $\times$ 22 bump bonded pixels (125 $\times$ 125 μm^2), one with p-stop rings and one with p-sprays (fig. 11.6). Irradiated pixels could not be tested reliably because we could not reach the operating temperature of -10° foreseen at CMS. During two weeks of beam time we collected some 6 $\times$ 10^6 events. The analog amplitudes from the pixels had first to be corrected for common mode noise. The hit coordinates for the strips and pixels were obtained from the average hits weighted by the hit amplitudes. After the alignment, the hit position of the incident particle on the pixel sensors was known with a (moderate) precision of $\approx 5\mu$m. Figure 11.7 shows the correlation between hit coordinates in the microstrips and pixel detectors.

The charge collected by one pixel depends on the incident track. On the borders of the pixel the charge is shared between few (mostly two) pixels, hence the collected charge in the tested pixel is smaller. The average charge collected by one pixel as a function of track position can be used to calculate the lateral charge diffusion in the silicon bulk. The charge distribution is a convolution of the charge diffusion function with the size of the pixel. The average charge collected by one pixel as a function of the track position in the x and y directions on the pixel surface is shown in fig. 11.8.

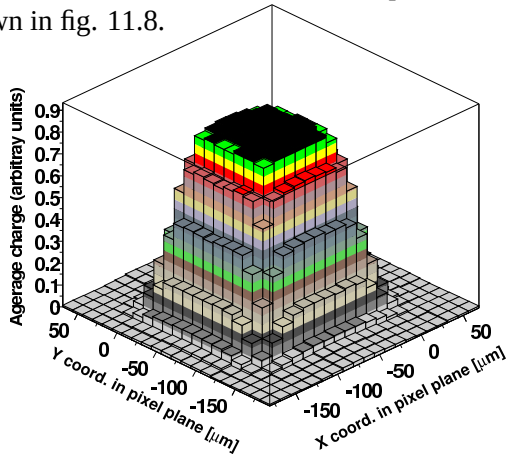

Figure 11.8: *Average collected charge by one pixel in the absence of magnetic field.*

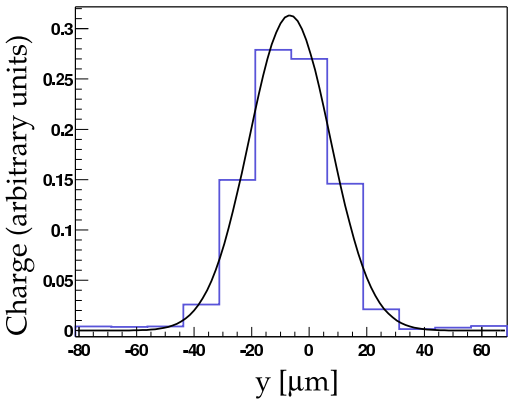

Figure 11.9: *Lateral charge distribution due to diffusion in the 280 μm thick silicon, together with gaussian fit.*

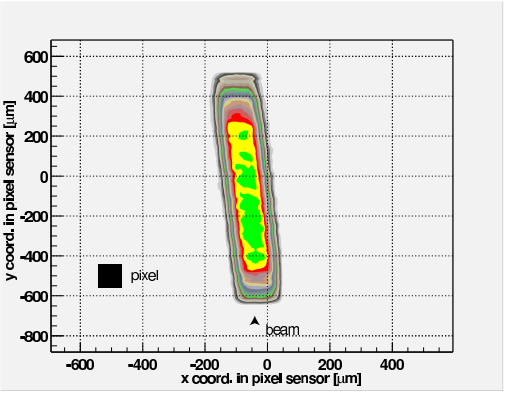

Figure 11.10: *Distribution of collected charge on the surface of the silicon sensor for grazing tracks. The y coordinate is along the beam direction.*

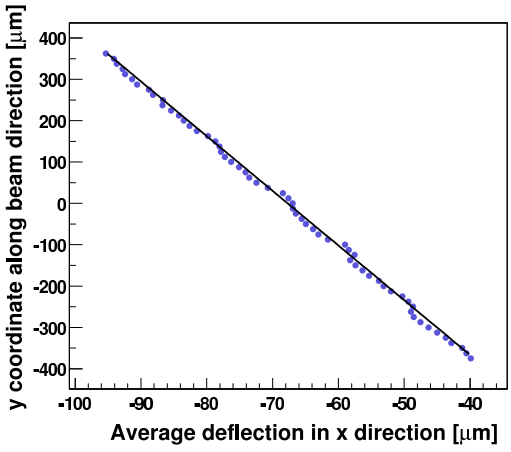

Figure 11.11: *Average deflection as a function of detected track length along the beam direction.*

The detector was oriented with its surface perpendicular to the incident beam and the magnetic field was off. The deconvoluted lateral charge distribution during the charge drift through the 280 μm thick silicon is shown in fig. 11.9, together with a gaussian fit. The lateral diffusion has an r.m.s. width of about 15 μm.

Figure 11.10 shows the distribution of charge with magnetic field. The pixel detector was oriented with its surface at a grazing angle of 15° and the field was 3 T. One can see that the charge migrates slightly to the left of the incident track. The coordinate of average energy deposit is shown in fig. 11.11 as a function of track length y. The Lorentz angle calculated for the non-irradiated sensor is about 16° at 3 T and 21° at 4 T.

Finally, we measured the position resolution of the pixel detector. In the CMS detector the tracks hitting the pixel barrel are on average perpendicular to the magnetic field. However, the field was parallel to the beam during our test. To simulate charge sharing due to the magnetic field, the detector surface was therefore tilted by an angle of 65° with respect to the beam direction to simulate the Lorentz deflection. In the vertical direction the charge was shared by several pixels while in the horizontal direction the charge was collected by single pixels (except for tracks in the border regions for which charge was collected by two adjacent pixels). The measured coordinate was obtained by weighting the pixel hits with their amplitudes. Figure 11.12 and 11.13 show the residuals between

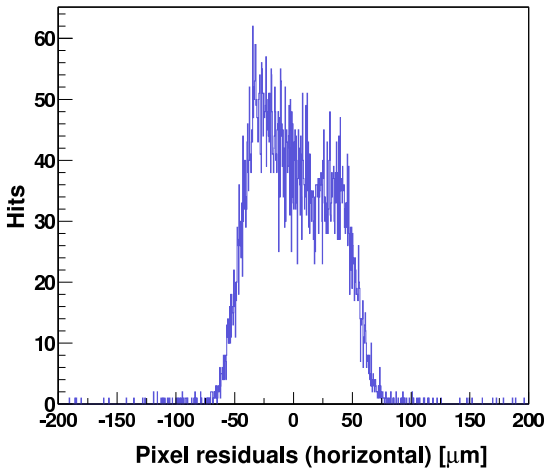

Figure 11.12: *Residuals between measured and predicted horizontal coordinates, showing the enhanced resolution obtained with charge division.*

measured and predicted hits from the telescope in the horizontal and vertical directions, respectively. In the horizontal direction the resolution is about $\sigma \simeq 34\mu$m, as expected from a box distribution for 125 μm broad pixels. In the vertical direction, however, the resolution is much better thanks to charge sharing: $\sigma \simeq 11\mu$m.
Another important aspect is the signal-to-noise ratio. The energy deposit for minimum ionizing particles was measured for perpendicular incidence. The resulting Landau distribution was compared to the (gaussian) noise distribution. We obtained a signal-to-noise ratio of 130.

[1] CMS - The Tracker Project, Technical Design Report, CERN LHCC 98-6, CMS TDR 5 (1998).

[2] R. Kaufmann, PhD Thesis, Universität Zürich, 2001.

[3] C. Amsler *et al.*, Nucl.Instr.Meth.**A 480** (2002) 501.

[4] B. Henrich and R. Kaufmann, Nucl.Instr.Meth.**A 304** (2002) 304.

[5] P. Billoir and S. Qian, Nucl.Instr.Meth.**A 311** (1992) 139.

11.2 Readout chip

During summer 2002 we also tested in a high intensity pion beam of 350 MeV/c at PSI the CMS Read Out Chip (ROC) which was designed in radiation hard DMILL technology. For that test we used the PSI43 chip, the first ROC that contained the complete functionality and the foreseen number of pixels (52 columns $\times$ 53 rows of pixels). We were able to test the chip-sensor unit under rates comparable to those expected at LHC.
In 2002 we also received our first test structures, which were processed in quarter micron technology (Deep Sub Micron, DSM). A complete redesign of the existing chip was necessary but this technology has the following advantages: DSM chips are cheaper since the process is well known and used widely by the conventional chip industry. DSM technology also offers new possibilities in designing the chip and improving its performances. There are for example five metal layers available for routing instead of only two and the smallest structure is only 0.25 μm wide, compared to 0.8 μm in DMILL. Thus

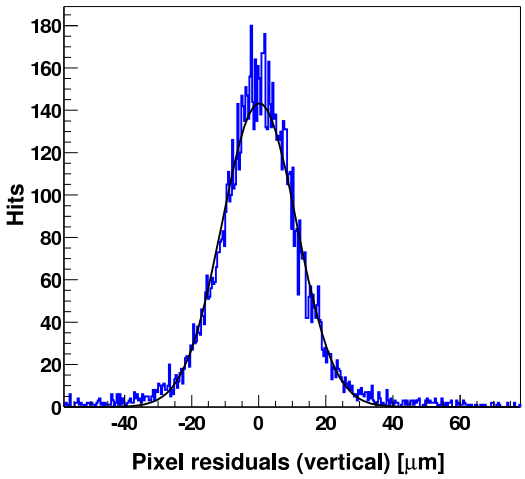

Figure 11.13: *Residuals between measured and predicted vertical coordinates, showing the enhanced resolution obtained with charge division.*

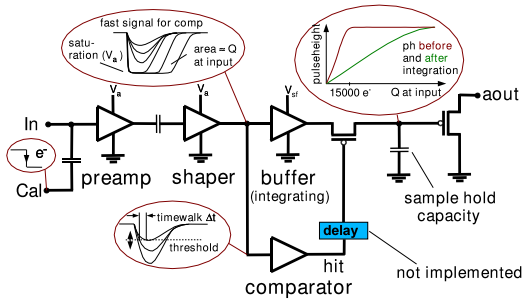

Figure 11.14: *Layout of the analog block test structure.*

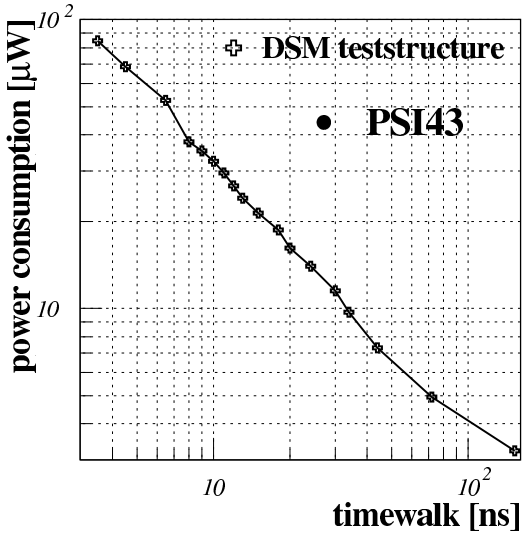

Figure 11.15: *Power consumption versus timewalk.*

we will be able to increase the number of data buffers from 24 to 32 and thereby reduce data loss. Another benefit is the low power consumption as DSM needs only half the supply voltage and half the current of DMILL. Thus, as will be shown below, the power consumption is four times lower for the same speed. We also expect a higher yield than in case of DMILL and the radiation hardness is excellent.

We have performed measurements with test structures of the analog block that were designed in DSM technology. Figure 11.14 shows the schematics of the analog block test structure.

It consists of two stages, a charge sensitive preamplifier and a shaper. Both stages have to be very fast because of the 40 MHz bunch crossing frequency at LHC. An extra amplifier integrates the signal to deal with saturated shaper output signals. These amplifier stages are followed by the sample and hold capacity and an output driver. A comparator, integrated in the analog block, generates the hit signal when the output level of the shaper is higher than the input threshold of the comparator. The hit signal is needed for storing the pulse height in the sample and hold capacity until the readout sequence is completed.

A very important measurement was power consumption versus timewalk (fig. 11.15). A low power consumption is important, because each μW/pixel leads to about 60 Watt for the entire pixel detector. As fig. 11.15 shows, power consumption decreases rapidly with timewalk. However, whenthe latter exceeds 25 ns the event is assigned to the wrong bunch crossing. For test structure A we obtained a power consumption of 14 μW for a timewalk of 25 ns. This is much smaller than for the DMILL design (40μW) advocated in the design report [1].

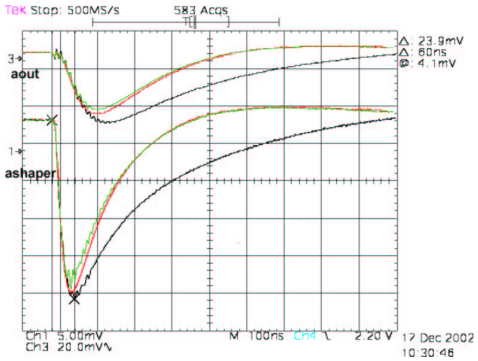

Figure 11.16: *Analog out of the shaper and aout (see also fig. 11.14) before (red) and after (black) irradiation, and after compensation (green).*

Figure 11.16 shows the output signal of the shaper and the analog output signal aout (see the layout in fig. 11.14) caused by a charge injected at the calibration input. The tests tructures were irradiated with a ^{60}Co γ-source (132 kGy) at PSI. The red curves were measured before irradiation, the black ones after radiation and the green ones after readjusting the settings for the preamp and shaper. Hence we were able to compensate for the irradiation damages, leading to an increase in gain and decay time, by readjusting the settings.

11.3 Mechanical support structure

Our group and our institute's workshop (see also the report from the mechanical workshop) are involved in the design and construction of the mechanical support structure for the detector and the service tube in beam direction. Figure 11.17 shows a sketch of a quarter of the CMS tracking system. The three layers of the pixel detector are shown, together with the 220 cm long service tube. The system has a total length of 5 m. Since the LHC beampipe will already be present during installation of the pixel detector, two vertically separated pixel half shells will be introduced on a dedicated rail system (see also fig. 11.22 below). The detector support structure (fig. 11.18) will be made of pure aluminum tubes with trapezoidal shapes to fit the geometrical constraints and a wall thickness of only 0.3 mm. Custom made, 0.24 mm thick, carbon fiber blades, which support the pixel modules, will then be glued to the tubes forming the detector segments. Four to five of these tubes will be connected

with a laser welding technique to an aluminum container which distributes the cooling fluid. Figure 11.19 shows a picture of such a welding seem taken with a microscope. Note that the width of the

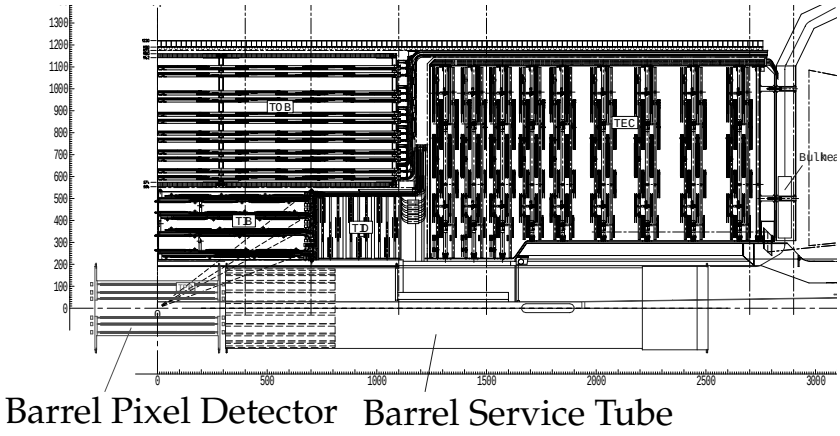

Figure 11.17: *A quarter of the CMS tracking system with the barrel pixel detector in the center and the service tube in z-direction.*

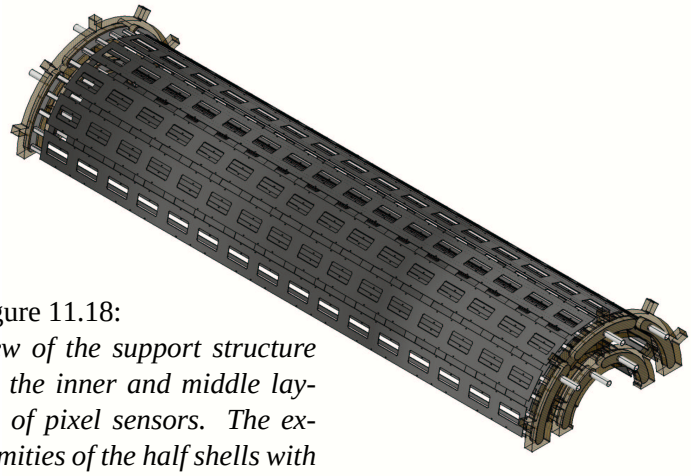

Figure 11.18:
View of the support structure for the inner and middle layers of pixel sensors. The extremities of the half shells with the embedded cooling manifolds are also shown.

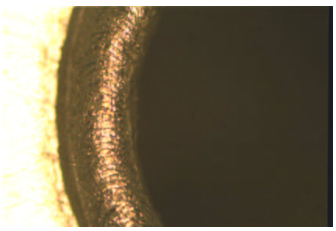

Figure 11.19: *High quality welding seem between a cooling tube (right side) and the container (left side).*

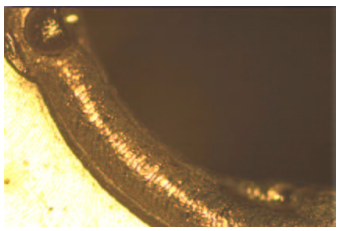

Figure 11.20: *Bad welding seem with a hole and a gap.*

seem is only about 0.3 mm. The resulting manifold will provide the necessary cooling of the detector modules to -10^{0}C with C_6F_{14}. At both ends the manifolds are embedded in a carbon fibre support frame as illustrated in fig. 11.18.
The laser welding is done in close collaboration with an external company. Tests gave promising results (fig. 11.19). However, we realized that the tool used was not precise nor massive enough. Figure 11.20 shows a problematic zone with holes and gaps. This happens when the laser beam misses the working piece or when there is an excessive gap between the parts that have to be welded. The tests indicated also that the physical and chemical properties of the different pieces have to be of the same quality. A complete detector segment was manufactured with an improved welding tool consisting of massive copper pieces supporting the segment structure during the welding process. The new tools guarantee the required precision and remove the heat during the welding process.

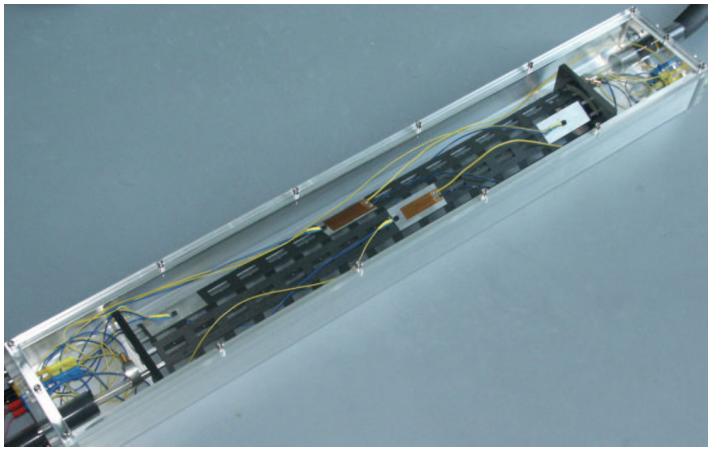

Figure 11.21: *Detector segment in its dry nitrogen container. Note the resistors to simulate the power loss and the temperature sensors mounted on the carbon fibre blades.*

The segment of the barrel pixel support structure was installed in a container and flushed with dry nitrogen for cooling tests (fig. 11.21). Mechanical survey and cooling tests will have to be performed to prove that the technique meets all requirements.

The two service tubes in $+z$ and $-z$ direction, which enclose the end cap pixel detector system (fig. 11.22), connect the barrel pixel detector to the tracking system. They transfer the power, the optical and electrical signals and the cooling fluid to the detector. To minimize multiple scattering we will use aluminum wires, which are plated with a thin copper layer for the power lines and aluminum for the cooling tubes. The motherboards which hold the optical hybrids for the analog and control links are integrated at the detector end. The power regulators are mounted at the outer ends. A honeycomb support structure is foreseen (fig. 11.23) to minimize the amount of material and to guarantee stability.

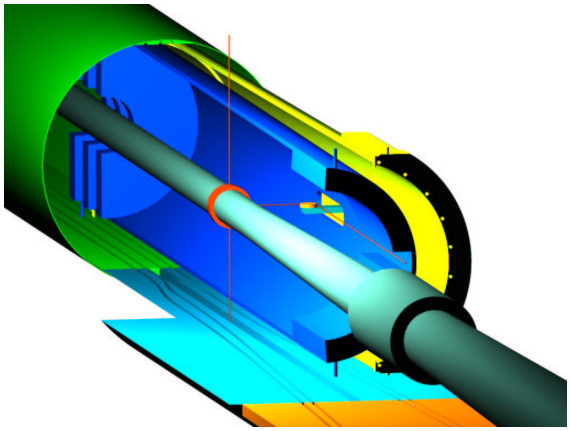

Figure 11.22: *The CMS beampipe surrounded by the pixel detector service tubes for the barrel detector (yellow) and the end cap discs (blue).*

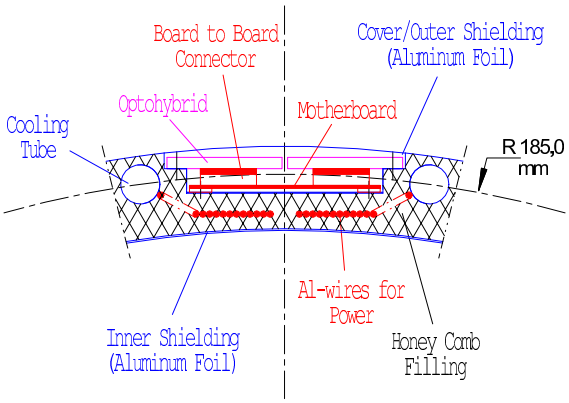

Figure 11.23: *Cross section of the service tube near the pixel detector flange, showing the motherboards which hold the optical hybrids.*

11.4 CMS event reconstruction

We are participating in the track reconstruction software and, in particular, in the vertex reconstruction techniques in the object-oriented reconstruction framework ORCA. We have implemented a single-vertex fit algorithm using the Kalman filter formalism. This algorithm is often used both in track [2] and vertex reconstruction [3].

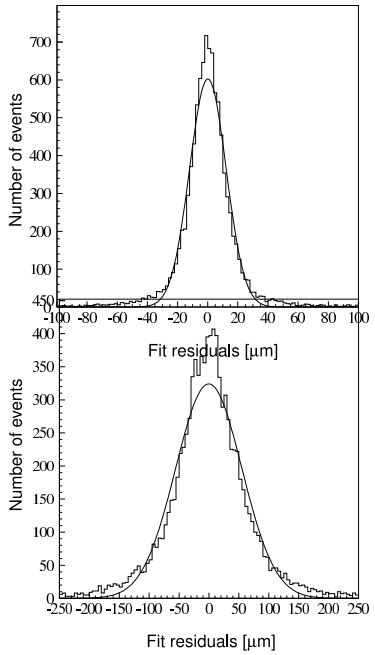

Figure 11.24: *Residuals distributions in the transverse direction for the decay vertex in $H^0 \rightarrow Z^0Z^0 \rightarrow \mu^+\mu^-\mu^+\mu^-$ (top) and in $B_s \rightarrow J/\psi\phi$ (bottom).*

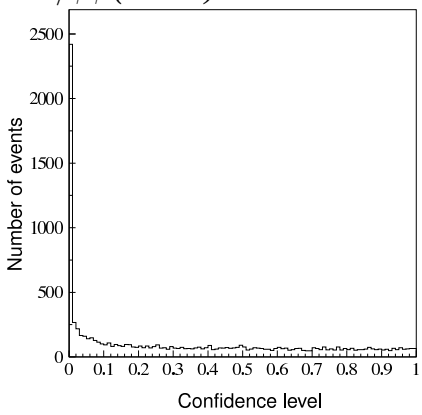

Figure 11.25: *Confidence level distribution expected for $H^0 \rightarrow Z^0Z^0 \rightarrow \mu^+\mu^-\mu^+\mu^-$.*

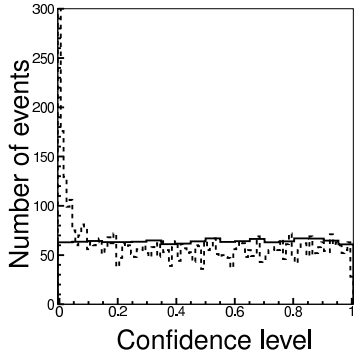

Figure 11.26: *Confidence level distribution for tracks with perfectly gaussian track parameters (full line) and tracks affected by 3% non-gaussian tails (dashed line).*

So far only a simplified version[4; 5] of a Kalman filter had been implemented. Tracks were assumed to be straight in the vertex neighbourhood. This considerably simplified the algorithm and reduced the computation time but did not allow the tracks to be refitted as emerging from a common vertex. In our improved version of the filter realistic helicoidal track models are used. Track parameters may then be recalculated with the additional vertex constraint, providing a full track-to-track covariance matrix.

The r.m.s.resolution of the reconstructed vertex in the decay $H^0 \rightarrow Z^0Z^0 \rightarrow \mu^+\mu^-\mu^+\mu^-$ is approximately 12 μm in the transverse and 19 μm in the longitudinal (z) direction. For B_s meson decays the resolutions are 55 μm and 73 μm, respectively (fig. 11.24). While no improvement is gained on the resolution, the full Kalman filter algorithm is up to four times faster than the linearized version. This is interesting in view of its possible application to the online high-level trigger.

Nevertheless, the distributions of the confidence level (fig. 11.25) show a large peak at low confidence level. This is due to the track parameters which have non-gaussian tails, as demonstrated in fig. 11.26. To alleviate this problem, we are developing a gaussian sum filter (GSF) for vertex fitting, in which the distributions of the track parameters are modelled by superpositions of gaussians describing the core and the tails. The GSF is then a weighted sum of several Kalman filters, and it can be implemented as a number of Kalman filters run in parallel.

We have started to develop a kinematic fit with additional constraints (such as masses of decaying particles, momentum and energy conservation) incorporated into the vertex fit. We are able to reconstruct intermediate particles coming from sequential decays by imposing kinematic constraints on the final state particles. For example one can reconstruct complete decay chains, such as the decays $B^- \rightarrow D^0 l^- \bar{\nu}_l$, followed by $D^0 \rightarrow K^-\pi^+$, $D^0 \rightarrow K^-\pi^+\pi^0$ or $D^0 \rightarrow K^-\pi^+\pi^-\pi^+$, where only the final longlived particles are reconstruced in the detector. This procedure can also improve the experimental resolutions.

[1] CMS - The Tracker Project, Technical Design Report, CERN LHCC 98-6, CMS TDR 5 (1998).

[2] R. Frühwirth, Nucl.Instr.Meth.**A 262** (1987) 444.

[3] R. Frühwirth, R. Kubinec, W. Mitaroff and M. Regler, Comp. Phys. Comm. **96** (1996) 189.

[4] V. Karimäki, "Effective Vertex Fitting", CMS note 1997/051.